

1 **Statistically Steady State Large-Eddy Simulations**
2 **Forced by an Idealized GCM: 1. Forcing Framework**
3 **and Simulation Characteristics**

4 **Zhaoyi Shen¹, Kyle G. Pressel², Zhihong Tan³, Tapio Schneider^{1,4}**

5 ¹Department of Environmental Science and Engineering, California Institute of Technology, Pasadena,
6 CA, USA.

7 ²Pacific Northwest National Laboratory, Richland, WA, USA.

8 ³Department of the Geophysical Sciences, University of Chicago, Chicago, IL, USA.

9 ⁴Jet Propulsion Laboratory, Pasadena, CA, USA.

10 **Key Points:**

11 • A framework in which LES is driven by large-scale forcing from a GCM is devel-
12 oped

13 • LES with large-scale forcing reaches steady states without nudging to thermody-
14 namic GCM profiles

15 • LES driven by the GCM is used to simulate different tropical cloud regimes across
16 the Walker circulation

17 **Abstract**

18 Using large-eddy simulations (LES) systematically has the potential to inform parameterizations of subgrid-scale (SGS) processes in general circulation models (GCMs), such
 19 as turbulence, convection, and clouds. Here we show how LES can be run to simulate
 20 grid columns of GCMs to generate LES across a cross-section of dynamical regimes. The
 21 LES setup approximately replicates the thermodynamic and water budgets in GCM grid
 22 columns. Resolved horizontal and vertical transports of heat and water and large-scale
 23 pressure gradients from the GCM are prescribed as forcing in the LES. The LES are forced
 24 with prescribed surface temperatures, but atmospheric temperature and moisture are
 25 free to adjust, reducing the imprinting of GCM fields on the LES. In both the GCM and
 26 LES, radiative transfer is treated in a unified but idealized manner (semi-gray atmosphere
 27 without water vapor feedback or cloud radiative effects). We show that the LES in this
 28 setup reaches statistically steady states without nudging to thermodynamic GCM pro-
 29 files. The steady states provide training data for developing GCM parameterizations.
 30 The same LES setup also provides a good basis for studying the cloud response to global
 31 warming.
 32

33 **Plain Language Summary**

34 Clouds and their feedbacks remain one of the largest uncertainties in predictions
 35 of future climate changes. High-resolution models can provide faithful simulations of clouds
 36 and their underlying turbulence in limited areas, but they have primarily been used in
 37 select locations, with limited success in reducing uncertainties in climate predictions. This
 38 study presents a framework for driving high-resolution simulations by a global climate
 39 model, which allows us to generate a library of high-resolution simulations across dif-
 40 ferent cloud regimes. The framework leverages the potential of high-resolution models
 41 to improve parameterizations of clouds and turbulence in climate models and to better
 42 understand the cloud feedback mechanisms.

43 **1 Introduction**

44 General circulation model (GCM) predictions of the equilibrium climate sensitivity
 45 (ECS)—the equilibrium global mean surface temperature change after doubling of
 46 CO₂ concentrations—range between 2 K and 5 K across climate models (?, ?). This 3 K
 47 uncertainty has remained virtually unchanged for forty years (?, ?), despite increases in
 48 the complexity of climate models and exponential increases in the computational power
 49 of high-performance computing (HPC) systems (?, ?). Similar uncertainties exist in the
 50 transient climate response (?, ?). The largest uncertainties in model projections of cli-
 51 mate change are traceable to the way in which these models represent boundary layer
 52 clouds and their climate feedbacks (?, ?, ?, ?, ?, ?, ?, ?, ?). The challenge posed by clouds
 53 is that, on the one hand, their dynamics depend on small-scale processes, such as three-
 54 dimensional turbulence and microphysics, but on the other hand, they respond to and
 55 shape larger-scale atmospheric circulations. Thus, in coarse resolution GCMs, boundary-
 56 layer turbulence, convection, and clouds must be parameterized in terms of a GCM's re-
 57 solved fields. Inadequacies of these parameterizations are at the core of climate model
 58 uncertainties.

59 At the same time as the physical and computational complexity of GCMs has in-
 60 creased, expanding HPC capabilities have also enabled high-resolution, limited-area mod-
 61 els, such as large-eddy simulations (LES), which directly resolve essential dynamics of
 62 turbulence, convection, and clouds. LES are being run with ever increasing resolution,
 63 on ever larger domains, and for ever longer durations. The ability of LES to provide high-
 64 fidelity simulations of boundary-layer turbulence, convection, and clouds is well estab-
 65 lished (?, ?, ?, ?, ?), making it a primary numerical laboratory for informing and vali-
 66 dating climate model parameterizations. However, LES have so far mostly been used in

67 selected locations, usually associated with field campaigns, such as the often studied BOMEX
 68 (?, ?), DYCOMS-II (?, ?), and RICO (?, ?) field campaigns. Some previous studies have
 69 used LES with idealized boundary conditions and large-scale forcings to investigate bound-
 70 ary layer dynamics in different dynamical regimes (e.g., ?, ?). Despite these attempts,
 71 the potential of LES to provide more systematic information for parameterizations across
 72 a broad cross-section of realistic dynamical regimes in a GCM has not been fully real-
 73 ized.

74 Here we describe an LES experimental design that allows us to explore a large range
 75 of atmospheric conditions encountered in a GCM. While driving limited-area models in
 76 idealized conditions in the tropics is well established (?, ?, ?), driving limited-area mod-
 77 els with large-scale forcing from a GCM or a numerical weather prediction model in prin-
 78 ciple can be done anywhere in the atmosphere. However, it is less well established how
 79 to do so; see the discussion of potential pitfalls in ? (?). A framework to drive LES with
 80 host models (GCMs or weather models) or reanalyses data is described by ? (?). In this
 81 framework, single-column models (SCMs) and/or LES are driven by prescribed large-
 82 scale forcing from host models or reanalyses, while being nudged toward the state of the
 83 host model or reanalysis. The nudging prevents the LES from drifting away from the
 84 host model or reanalysis state. But it also constrains the turbulence developed by the
 85 LES, which limits the independent insights that can be gained from the LES in some dy-
 86 namical regimes. Some early studies have investigated subtropical low cloud response
 87 to climate change with two-dimensional LES driven by prescribed large-scale forcings
 88 from a superparameterized GCM, while moisture nudging and adjustment of vertical mo-
 89 tions are used to prevent model drift (?, ?, ?). The large-scale forcing approach has been
 90 used in recent years to study boundary layer dynamics and cloud feedbacks in selected
 91 locations and over long times (e.g., ?, ?, ?, ?). Another approach to force LES with GCMs
 92 is one-way nesting (e.g., ?, ?, ?), where states at lateral boundaries of the LES domain
 93 are relaxed toward those in a host model. The nesting approach allows for heterogeneous
 94 boundaries. But it requires LES on large domains, which is computationally expensive.
 95 In this study, we drive LES by dynamically consistent large-scale forcings given by a GCM
 96 and allow LES to evolve freely, without nudging of thermodynamic variables in the at-
 97 mosphere. We use the LES systematically to simulate clouds in different dynamical regimes.

98 To prove the concepts and for simplicity in illustrating them, the GCM here is the
 99 idealized moist GCM used in a number of studies of large-scale dynamics going back to
 100 ? (?) and ? (?). The GCM has simplified radiation and convection schemes, and there
 101 are no clouds in the model. We treat each LES as representing an idealized single grid
 102 column of the host GCM by prescribing terms in the water and thermodynamic budgets
 103 resolved by the GCM as forcing within the LES. The treatment of radiative transfer is
 104 identically simplified between the LES and GCM, allowing the LES to achieve a phys-
 105 ically realizable atmospheric energy balance that is consistent with the GCM (albeit not
 106 necessarily realistic). Because the GCM's resolved-scale fluxes that are applied to the
 107 LES do not directly include contributions from parameterized turbulent and convective
 108 processes in the GCM, the LES responds by generating a turbulent flow that closes the
 109 budgets. To the extent that the parameterizations in the GCM are an accurate repre-
 110 sentation of the dynamics resolved by the LES, the LES and GCM should reach the same
 111 statistically steady states. The extent to which they do not do so reflects inadequacies
 112 in the parameterizations in the GCM, and the mismatches can be used to improve the
 113 parameterizations.

114 One unique aspect of this experimental design is that it allows an iterative work-
 115 flow to refine parameterizations that are implemented in a GCM. The iterative work-
 116 flow consists of the following steps:

- 117 1. Integrate the GCM to generate forcing data from selected GCM grid columns.
- 118 2. Integrate LES driven by forcing from the GCM columns.

119 3. Improve the GCM parameterizations by minimizing mismatches between the LES
 120 and the GCM simulations for the selected columns.
 121 4. Go to step 1.

122 GCM parameterizations can learn from offline LES simulations using data assim-
 123 ilation and machine learning approaches, and eventually, this workflow may be automated
 124 by spinning LES off the GCM simulation. Furthermore, experimental design approaches
 125 can be used to optimize the selection of GCM grid columns so as to be maximally in-
 126 formative about the parameterizations (?, ?). We do not demonstrate this workflow in
 127 this paper; rather, this paper is a contribution within a larger research program with the
 128 goal to realize such an automated workflow.

129 The rest of the paper is organized as follows. Section 2 discusses the GCM and LES
 130 used to simulate the transition from shallow to deep convection across a Walker circu-
 131 lation. Section 3 describes how the GCM grid column budgets of temperature and wa-
 132 ter vapor are decomposed and then used to force the LES. Section 4 describes the sim-
 133 ulation characteristics in this forcing framework. Section 5 summarizes the conclusions
 134 and discusses the potential application of this framework to a range of cloud-climate prob-
 135 lems.

136 **2 Model Descriptions**

137 **2.1 Moist Idealized General Circulation Model**

138 The GCM simulations used in this work are performed using the moist idealized
 139 GCM described in ? (?) and ? (?). Moist convective processes are represented using a
 140 simplified quasi-equilibrium (Betts–Miller) scheme (?, ?), which assumes convection re-
 141 laxes convectively unstable profiles towards moist-adiabatic reference profiles with a rel-
 142 ative humidity of 70%. Precipitation is formed both by the parameterized convection and
 143 by large-scale condensation when a GCM grid box reaches saturation. Only liquid wa-
 144 ter (rain) is considered, and precipitation is assumed to fall instantaneously to the sur-
 145 face. There are no clouds in the GCM. A k -profile eddy diffusivity scheme similar to that
 146 developed by ? (?), with a dynamically determined boundary layer height, is used to model
 147 turbulent transport within the atmospheric boundary layer. The atmosphere is assumed
 148 to overlay a 40-m deep slab ocean, with which it interacts through radiative transfer and
 149 through latent and sensible heat fluxes. Surface fluxes of heat, moisture, and momen-
 150 tum are modeled using bulk aerodynamic formulas with drag coefficients determined from
 151 Monin-Obukhov similarity theory, with a roughness lengths of 1×10^{-5} m for all quan-
 152 tities. Atmospheric radiative transfer is represented by a two-stream semi-gray radia-
 153 tion scheme, where longwave and shortwave absorption is calculated using prescribed lat-
 154 itudinally dependent absorber profiles, as described in ? (?). The model does not have
 155 seasonal cycles or diurnal cycles.

156 The GCM simulations we perform are of a zonally asymmetric aquaplanet, in which
 157 zonal asymmetry is imparted by prescribing an ocean heat flux divergence (see ??). The
 158 prescribed ocean heat flux divergence produces an off-equatorial Walker circulation, with
 159 suppressed convection in the region of maximum ocean heat flux divergence and enhanced
 160 convection in the region of maximum ocean heat flux convergence. Having a Walker cir-
 161 culation allows the LES driven by the aquaplanet GCM to generate somewhat more re-
 162 alistic tropical cloud regimes than would be possible in a zonally symmetric setting. The
 163 GCM is run at T42 horizontal spectral resolution with 72 vertical levels (30 levels in the
 164 lowest 1.5 km) for a total of 3000 days. We accumulate forcing data to drive the LES
 165 from the last 500 days of the simulation. The dipole pattern of the prescribed ocean heat
 166 flux divergence (Figure ??a) induces zonal variations in surface temperatures (Figure ??b)
 167 in the GCM. The zonally varying surface temperatures in turn drive an atmospheric Walker
 168 circulation, with strong ascent over warm temperatures and large-scale subsidence over

169 cold temperatures (Figure ??). To drive the LES, we extract forcing data from selected
 170 GCM grid-columns along a transect connecting the points of maximum and minimum
 171 ocean heat flux divergence (dots in Figure ??a).

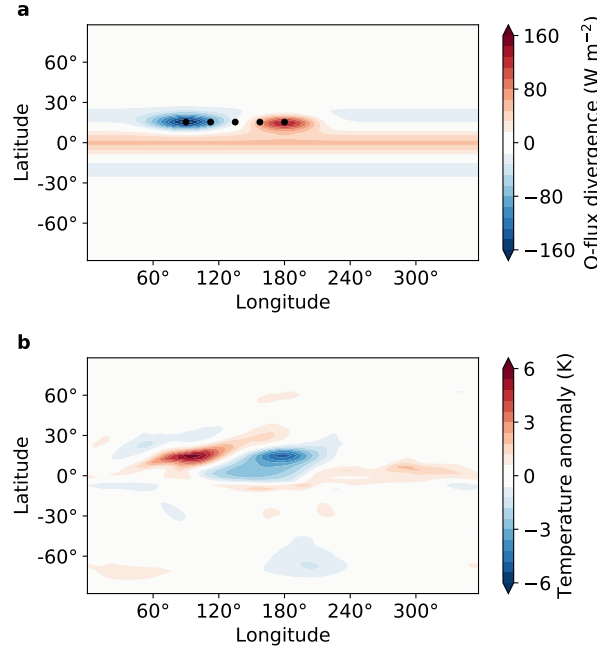


Figure 1. Surface fields in the GCM simulation. (a) Ocean heat flux divergence. (b) Surface temperature anomaly about zonal mean. Black circles indicate GCM grid columns along a transect connecting the regions of maximum and minimum ocean heat flux divergence.

172 2.2 Large-Eddy Simulation

173 The forcing framework is implemented in the Python Cloud Large-Eddy Simula-
 174 tion (PyCLES) code (?, ?). PyCLES is a parallel, three-dimensional LES code that solves
 175 the moist anelastic equations of motion (?, ?), with prognostic equations for moist spe-
 176 cific entropy s , total non-precipitating water specific humidity q_t , precipitating liquid wa-
 177 ter q_r (rain), and precipitating frozen water q_s (snow). The total water specific humid-
 178 ity includes contributions from water vapor q_v , non-precipitating liquid water q_l , and non-
 179 precipitating ice q_i , which are assumed to be in thermodynamic equilibrium. Along with
 180 dry air, these four components make up the thermodynamic system. The precipitating
 181 species are not assumed to be in thermodynamic equilibrium with q_t .

182 In PyCLES, the equations of motion are solved on a staggered, Arakawa-C grid (?,
 183 ?). The advection of both scalar and momentum fields are discretized using nominally
 184 fifth-order weighted essentially non-oscillatory (WENO) schemes implemented as described
 185 in ? (?) and based on the schemes developed by ? (?). Because of grid staggering, the
 186 actual accuracy of the WENO schemes is limited to second order. The pressure is di-
 187 agnosed following ? (?), and time-stepping is performed using a second-order strong sta-
 188 bility preserving Runge-Kutta scheme (?, ?). The numerical formulation does not en-
 189 sure monotonicity or positivity of solutions, so clipping is employed when needed to en-
 190 sure that fields such as specific humidities that need to remain positive do indeed remain
 191 positive. Subgrid-scale (SGS) fluxes of momentum and scalars are modeled through the
 192 Smagorinsky-Lilly closure (?, ?, ?), with the Smagorinsky coefficient $c_s = 0.17$ and the

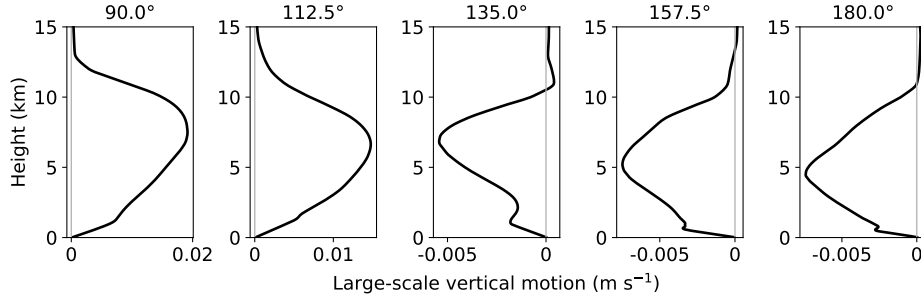


Figure 2. Vertical profiles of large-scale vertical motion in the GCM along the Walker circulation transect. The longitudes of the simulations are indicated above each panel.

turbulent Prandtl number $\text{Pr}_t = 1/3$. A Rayleigh friction sponge layer near the LES top is used to absorb waves, with horizontal velocities damped toward the domain mean with the height-dependent damping coefficient described in ??.

The formation and fate of precipitating species is represented using a single-moment, bulk microphysical model based on the scheme developed by ? (?); differences between their scheme and that used here are enumerated in ???. Precipitation that reaches the surface is assumed to fall out of the atmosphere, with no transfer of energy or mass to the ocean. The LES are forced with prescribed sea surface temperatures from the GCM. It is tempting to allow the surface temperatures in LES to vary by coupling the simulations with a slab ocean; however, we found that doing so leads to significant drift of the LES away from the GCM state in deep convection regions, presumably because of inadequacies of the simple turbulence and convection parameterizations employed in the GCM. Surface fluxes are modeled using bulk aerodynamic formulas based on Monin-Obukhov similarity theory. Radiative transfer is represented identically to the scheme used in GCM, with no effects of clouds on the radiative transfer.

We run LES driven by the GCM fields into a statistically steady state. This is computationally expensive for several reasons. First, we simulate a large, three-dimensional, doubly periodic domain that is 64 km wide and 25.6 km high, to be able to simulate deep convection. Second, the timescale for the LES to reach a statistically steady state is set by the timescale over which the atmosphere equilibrates, which can take tens of days. To reduce the computational cost we run the LES at a relatively coarse resolution of 250 m. The vertical grid is stretched and consists of 256 grid points. The vertical resolution decreases from about 50 m near the surface to around 200 m at the domain top. The simulations are run for 60 days (90.0° and 112.5°), 90 days (135.0°), or 180 days (157.5° and 180.0°). The results in this study are averaged over the last 15 simulated days, when the simulations have reached statistically steady states.

3 Forcing Framework

3.1 GCM Equations

Our goal is to develop an LES forcing framework in which the LES emulates a single grid column of a GCM, directly resolving processes that are parameterized in the GCM while satisfying the same large-scale water and thermodynamic balances as the GCM. To achieve this, we begin by considering the equations for the grid-scale temperature \tilde{T} and specific humidity \tilde{q}_t that are resolved by the GCM. Tildes ($\tilde{\cdot}$) denote variables resolved on the GCM grid. The thermodynamic equation in the GCM's σ coordinates is

227 given by (?, ?)

$$228 \quad \underbrace{\partial_t \tilde{T} + \tilde{u} \partial_x \tilde{T} + \tilde{v} \partial_y \tilde{T} + \tilde{\omega} \partial_\sigma \tilde{T} - \frac{\tilde{\alpha} \tilde{\omega}}{c_p}}_{\text{GCM-Resolved Dynamics}} = \underbrace{\tilde{J}_{\text{conv}} + \tilde{J}_{\text{cond}} + \tilde{J}_{\text{diff}} + \tilde{J}_{\text{numerical}} + \tilde{J}_{\text{rad}}}_{\text{GCM Parameterized}}, \quad (1)$$

229 which we have written such that the left hand side of the equation is the sum of the time-
 230 tendency of temperature and GCM-resolved advection terms, while the right hand side
 231 consists of parameterized source terms arising from the deep convection scheme (\tilde{J}_{conv}),
 232 large-scale condensation (\tilde{J}_{cond}), diffusive parameterizations such as the boundary layer
 233 turbulence scheme (\tilde{J}_{diff}), the radiation scheme (\tilde{J}_{rad}), and numerical damping and spec-
 234 tral filtering ($\tilde{J}_{\text{numerical}}$). Here, $\sigma = \tilde{p}/\tilde{p}_s$, with pressure \tilde{p} and surface pressure \tilde{p}_s , $\tilde{\omega} =$
 235 $d\sigma/dt$, $\tilde{\omega} = d\tilde{p}/dt$, $\tilde{\alpha}$ is the specific volume, and c_p is the specific heat capacity of dry
 236 air; the notation is otherwise standard. (We use Cartesian coordinates to simplify the
 237 notation; however, the GCM uses spherical coordinates, whereas the LES is Cartesian.)
 238 Similarly, the GCM's specific humidity budget is given by

$$239 \quad \partial_t \tilde{q}_t + \underbrace{\tilde{u} \partial_x \tilde{q}_t + \tilde{v} \partial_y \tilde{q}_t + \tilde{\omega} \partial_\sigma \tilde{q}_t}_{\text{GCM-Resolved Dynamics}} = \underbrace{\tilde{S}_{\text{conv}} + \tilde{S}_{\text{cond}} + \tilde{S}_{\text{diff}}}_{\text{GCM Parameterized}}. \quad (2)$$

240 In a statistically steady state, the explicit time derivatives vanish upon long-term
 241 time averaging, and the parameterized processes on the right-hand sides balances with
 242 resolved-scale flows of \tilde{T} and \tilde{q}_t on the left-hand sides. Our goal is to impose the resolved-
 243 scale budget terms on the left-hand side of equations (??) and (??) on the LES, while
 244 allowing the LES to generate a three-dimensional turbulent flow, microphysical processes,
 245 and radiative energy fluxes that determine the terms on the right-hand sides of the same
 246 equations. Here we implement long-time mean forcing from statistically steady states
 247 of the GCM, without the explicitly time dependent terms; however, it is straightforward
 248 to drive the LES using time-varying forcing from the GCM consistent with equations (??)
 249 and (??). We limit the present study to simulations using long-time mean forcing be-
 250 cause time varying forcing includes synoptic scale variability which would require much
 251 longer LES simulations to achieve statistically robust results.

252 3.2 Specific Humidity Forcing

253 In the LES, we modify the prognostic equation for total water specific humidity
 254 to include additional source terms S_{hadv} and S_{vadv} arising from GCM-resolved horizon-
 255 tal and vertical advection, giving

$$257 \quad \partial_t q_t + \partial_x (u q_t) + \partial_y (v q_t) + \rho_0^{-1} \partial_z (\rho_0 w q_t) = -\partial_x (\gamma_{q,x}) - \partial_y (\gamma_{q,y}) - \rho_0^{-1} \partial_z (\rho_0 \gamma_{q,z}) \\ 258 \quad + E - P + S_{\text{hadv}} + S_{\text{vadv}}, \quad (3)$$

260 where ρ_0 is the reference density, $\gamma_{q,x}$, $\gamma_{q,y}$, and $\gamma_{q,z}$ are the SGS fluxes of q_t , and E and
 261 P are source terms due to evaporation and production of hydrometeors. Consistent with
 262 ? (?), we prescribe the horizontal advective source term directly from the GCM such that

$$263 \quad S_{\text{hadv}} = -\langle \tilde{u} \partial_x \tilde{q}_t \rangle - \langle \tilde{v} \partial_y \tilde{q}_t \rangle, \quad (4)$$

264 where $\langle \cdot \rangle$ indicates a long-time mean on σ surfaces in the statistically steady state of the
 265 GCM.

266 Specification of the vertical advection source term is more complicated because the
 267 LES produces its own vertical advection, acting on its own domain-mean vertical gra-
 268 dients. We compute the vertical advection source term by rewriting the vertical advec-
 269 tion term in equation (??) using the hydrostatic relation and decomposing it into time
 270 mean and fluctuating components as

$$271 \quad \langle \tilde{\omega} \partial_\sigma \tilde{q}_t \rangle \approx \langle \tilde{w} \rangle \partial_z \langle \tilde{q}_t \rangle + \langle \tilde{w}' \partial_z \tilde{q}'_t \rangle, \quad (5)$$

272 where $w = dz/dt$ is the vertical velocity and primes $(\cdot)' = (\cdot) - \langle \cdot \rangle$ denote fluctuations
 273 about the time mean $\langle \cdot \rangle$. We approximate the time-averaged vertical velocity by $\langle \tilde{w} \rangle \approx$
 274 $-\langle \tilde{\omega} \rangle \langle \tilde{\alpha} \rangle / g$ where we have assumed that $\tilde{\omega}$ and $\tilde{\alpha}$ are uncorrelated. Replacing the GCM
 275 specific humidity \tilde{q}_t with the LES specific humidity q_t then gives the vertical advection
 276 source term we apply to the LES:

$$277 \quad S_{\text{vadv}} = -\langle \tilde{w} \rangle \partial_z q_t - \langle \tilde{w}' \partial_z \tilde{q}_t' \rangle. \quad (6)$$

278 The first term on the right-hand side accounts for vertical advection of q_t by GCM-resolved
 279 time-mean vertical motion. The second term accounts for vertical fluxes associated with
 280 fluctuations about the long-time mean and is prescribed directly from the GCM; it is typ-
 281 ically much smaller than the mean component.

282 3.3 Specific Entropy Forcing

283 We modify the LES prognostic equation for moist specific entropy to include source
 284 terms owing to GCM-resolved transports of total water specific humidity and temper-
 285 ature, such that

$$287 \quad \partial_t s + \partial_x (us) + \partial_y (vs) + \rho_0^{-1} \partial_z (\rho_0 ws) = -\partial_x (\gamma_{s,x}) - \partial_y (\gamma_{s,y}) - \rho_0^{-1} \partial_z (\rho_0 \gamma_{s,z}) \\ 288 \quad + \frac{c_p}{T} J_{\text{rad}} + \dot{S} + \frac{c_p}{T} (J_{\text{hadv}} + J_{\text{vadv}}) + (s_v - s_d) (S_{\text{hadv}} + S_{\text{vadv}}), \quad (7)$$

290 where $\gamma_{s,x}$, $\gamma_{s,y}$, and $\gamma_{s,z}$ are the SGS fluxes of s and J_{rad} is the source term due to
 291 radiation. The term \dot{S} represents irreversible entropy sources associated with the SGS dy-
 292 namics and precipitation processes, as described in ? (?). The last two terms on the right-
 293 hand side arise from the GCM-resolved advective tendencies of temperature (J_{hadv} and
 294 J_{vadv}) and total water specific humidity (S_{hadv} and S_{vadv}), and s_v and s_d are specific
 295 entropies of dry air and water vapor, respectively. Consistent with ? (?) and the treat-
 296 ment of total water specific humidity in section ??, we take the horizontal advective tem-
 297 perature tendency J_{hadv} directly from the GCM, such that

$$298 \quad J_{\text{hadv}} = -\langle \tilde{u} \partial_x \tilde{T} \rangle - \langle \tilde{v} \partial_y \tilde{T} \rangle + \langle \tilde{J}_{\text{numerical}} \rangle. \quad (8)$$

299 The vertical advective temperature tendency J_{vadv} , including the pressure-volume work
 300 term $\tilde{\alpha} \tilde{\omega} / c_p$, is derived by using the hydrostatic approximation to approximate the last
 301 term on the left-hand side of (??),

$$302 \quad \left\langle \tilde{\omega} \partial_\sigma \tilde{T} - \frac{\tilde{\alpha} \tilde{\omega}}{c_p} \right\rangle \approx \langle \tilde{w} \rangle \partial_z \langle \tilde{T} \rangle + \langle \tilde{w}' \partial_z \tilde{T}' \rangle + \langle \tilde{w} \rangle \frac{g}{c_p}. \quad (9)$$

303 Here, we have used again the approximation $\langle \tilde{w} \rangle \approx -\langle \tilde{\omega} \rangle \langle \tilde{\alpha} \rangle / g$. Replacing the GCM
 304 temperature \tilde{T} with the LES temperature T in the first term on the right-hand side then
 305 gives the vertical transport applied to the LES as

$$306 \quad J_{\text{vadv}} = -\langle \tilde{w} \rangle \partial_z T - \langle \tilde{w}' \partial_z \tilde{T}' \rangle - \langle \tilde{w} \rangle \frac{g}{c_p}, \quad (10)$$

307 with the second and third terms on the right-hand side taken directly from the GCM.

308 While we have discussed the forcing framework for an LES using specific entropy
 309 as a prognostic variable, it is straightforward, and in some ways easier, to implement it
 310 in models using other formulations of moist thermodynamics. For example, in an LES
 311 using some variety of liquid-ice potential temperature as a prognostic variable, the for-
 312 mulation of the specific humidity forcing is identical to that described here, and the GCM-
 313 resolved transport terms in the potential temperature equations are analogous to the terms
 314 involving $J_{\text{hadv/vadv}}$ on the right-hand side of equation (??) but with the inverse Exner
 315 function replacing $1/T$.

316 **3.4 Momentum Forcing**

317 The LES horizontal momentum field is driven by the large-scale pressure gradient
 318 from the GCM and Coriolis acceleration. The LES horizontal momentum equations are
 319 modified to be
 320

$$321 \partial_t u + \partial_x (uu) + \partial_y (uv) + \rho_0^{-1} \partial_z (\rho_0 uw) = -\partial_x (\rho_0^{-1} p') \\ 322 \quad - \partial_x \tau_{xx} - \partial_y \tau_{xy} - \rho_0^{-1} \partial_z (\rho_0 \tau_{xz}) - f (\langle \tilde{v}_g \rangle - v), \quad (11)$$

324 and
 325

$$326 \partial_t v + \partial_x (uv) + \partial_y (vv) + \rho_0^{-1} \partial_z (\rho_0 vw) = -\partial_y (\rho_0^{-1} p') \\ 327 \quad - \partial_x \tau_{yx} - \partial_y \tau_{yy} - \rho_0^{-1} \partial_z (\rho_0 \tau_{yz}) + f (\langle \tilde{u}_g \rangle - u) \quad (12)$$

329 where τ represents the SGS stress, and $\langle \tilde{u}_g \rangle$ and $\langle \tilde{v}_g \rangle$ are the mean zonal and meridional
 330 geostrophic winds from the GCM.

331 The prescribed momentum forcing leads to strong inertial oscillations in upper troposphere in the LES. In order to reduce the magnitude of the oscillation, the LES mean
 332 horizontal winds are relaxed to GCM mean in the free troposphere, with a timescale of
 333 2 days.
 334

335 **3.5 Radiation**

336 One essential aspect of this framework is that the representation of radiative transfer
 337 implemented in the LES should be identical to that implemented in the GCM. This
 338 enables controlled numerical experiments that isolate differences between resolved tur-
 339 bulence, convection, and clouds in the LES from their parameterized counterparts in the
 340 GCM. Furthermore, using the same representation of radiative transfer guarantees that,
 341 at least initially, free-troposphere large-scale transport imposed on the LES from the GCM
 342 is balanced by radiative heating/cooling, thus preventing the free-troposphere temper-
 343 ature from drifting. This is why we employ the same two-stream gray radiation scheme,
 344 without cloud radiative effects, in both the LES and the GCM.

345 **3.6 Surface fluxes**

346 Surface fluxes are modeled using a bulk scheme with drag coefficients obtained from
 347 Monin-Obukhov similarity theory (?). Since we are using the time-mean forcing from
 348 the GCM, the variation in surface wind speed in the LES is much smaller than in the
 349 GCM. This leads to significant differences in surface fluxes between the GCM and LES,
 350 which affects the temperature profile. To account for synoptic variability, we modify the
 351 surface wind speed to add a gustiness when calculating surface fluxes in the LES. The
 352 gustiness is estimated by the standard deviation of 6-hourly wind speed at the lowest
 353 model level in the GCM, which decreases from 3.20 m s^{-1} over the warmest surface tem-
 354 perature to 1.49 m s^{-1} over the coldest surface temperature.

355 **3.7 Interpolation**

356 The GCM and LES use different vertical grids (σ vs. z coordinates). Therefore, ver-
 357 tical profiles extracted from the GCM must be interpolated onto the LES vertical grid.
 358 We do so by interpolating from the GCM's σ levels onto the LES's height levels using
 359 the time-mean height of each σ level at the horizontal location in question. This repre-
 360 sents an additional approximation because averages at constant σ and constant z dif-
 361 fer. One of two interpolation methods is used depending on whether the gradient of the
 362 interpolated field appears explicitly in the forcing. For variables that do not appear in-
 363 side a gradient (e.g., u , v , or J_{hadv}), the GCM profiles are interpolated using a mono-

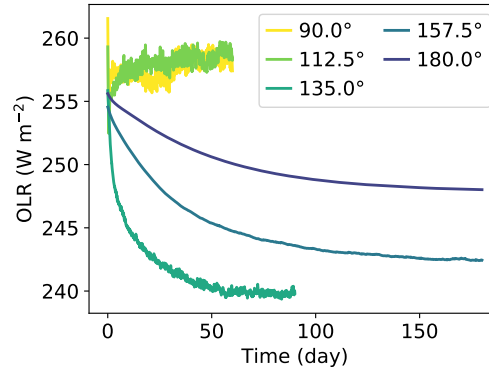
364 tonic piecewise cubic Hermite interpolating polynomial (PCHIP). For interpolated vari-
 365 ables that do appear inside a gradient (e.g., q_t or T), the vertical derivative of the field
 366 on the GCM grid is interpolated to the LES vertical grid using a PCHIP interpolation,
 367 and the value of the field is recovered by numerically integrating the interpolated deriva-
 368 tive using the trapezoidal rule. This approach ensures a nearly monotonic interpolation
 369 of discrete derivatives of the field.

370 3.8 LES Initial Condition

371 The LES initial conditions are specified from the GCM statistically steady-state
 372 mean vertical profiles of temperature, specific humidity, and horizontal geostrophic wind
 373 speed. Starting with this initial condition helps because it ensures that where param-
 374 eterized processes in the GCM vanish, the GCM-resolved forcing terms balance (up to
 375 small differences arising mostly from numerical interpolation error), provided the treat-
 376 ment of radiative transfer is identical in both models.

377 4 Simulation Characteristics

378 Figure ?? shows the timeseries of outgoing longwave radiation in the LES and il-
 379 lustrates the time it takes to equilibrate to a statistically steady state. The simulations
 380 reach steady state more rapidly in deep convection regions than in shallow convection
 381 regions, and all cases are in statistically steady state by the end of the simulations. As
 382 the LES are free to evolve from their initial condition, which is specified to be the long-
 383 time mean of the GCM, their equilibrated solution can diverge substantially from their
 384 initial state. The differences between the equilibrated LES solution and GCM long-time
 385 means can be used to identify deficiencies in GCM parameterizations.



386 **Figure 3.** Timeseries of LES outgoing longwave radiation (OLR) at various longitudes along
 387 the Walker circulation transect.

388 Figure ?? shows the equilibrium temperature and relative humidity profiles in the
 389 GCM and in the LES along the Walker circulation transect. The temperature profiles
 390 are in general very similar between the GCM and LES, except that in the free troposphere
 391 the LES is slightly cooler than the GCM at 135.0° longitude, which is consistent with
 392 the lower OLR in the LES (Figure ??). There are larger differences in the relative hu-
 393 midity profiles. The GCM-simulated relative humidity in deep convection regions is close
 394 to 70% in the free troposphere. The relative humidity has a local maximum of about 90%
 395 near 1 km and decreases to about 60% near the surface. The relative humidity in the
 396 LES is higher than that in the GCM both in the free troposphere and near the surface.
 397 The difference in relative humidity between GCM and LES arises because in deep con-

396 vection regions, convection is occurring most of the time, and the difference shows the
 397 deficiency of the simple GCM convection scheme. In the LES, convection keeps the relative
 398 humidity at a high value, while in the GCM, the simple convection scheme keeps the relative
 399 humidity close to the reference value (0.7). The jump in relative humidity
 400 at about 5 km in the LES results from the cooling effect of snow melting. In shallow con-
 401 viction regions, the relative humidity in the GCM has local maxima near the surface and
 402 the tropopause and a local minimum in the middle of the troposphere. The LES pro-
 403 duces a much moister free troposphere at 135.0° longitude, which may be related to the
 404 lower tropospheric temperature in the LES. The differences between the GCM and LES
 405 at 135.0° longitude may partially result from the lack of coupling to large-scale motions
 406 in the LES. The simulations with lower surface temperatures (157.5° and 180.0°) in gen-
 407 eral resemble the GCM, with a slightly larger relative humidity in the LES.

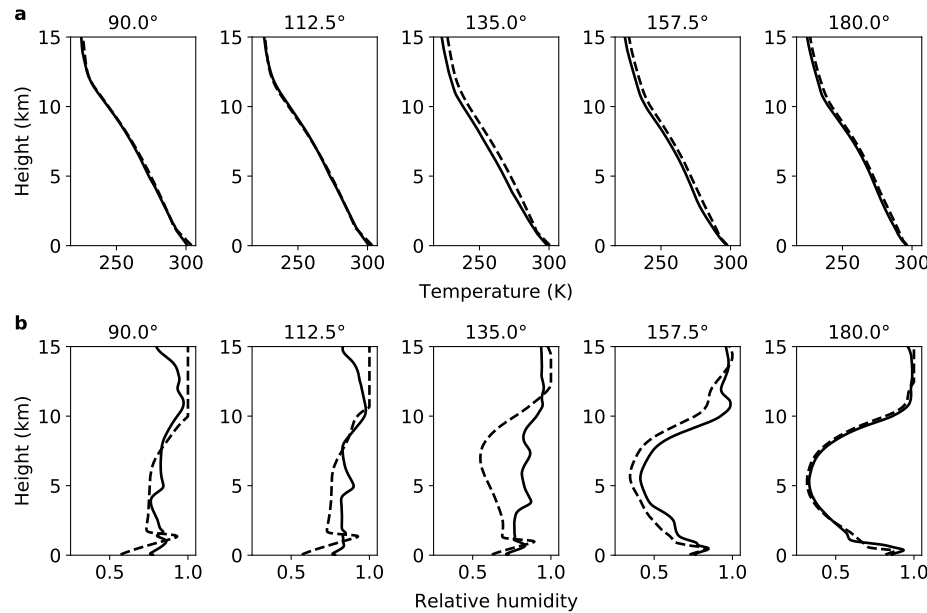


Figure 4. Vertical profiles of (a) temperature and (b) relative humidity along the Walker circulation transect in the GCM (dashed) and in the LES (solid). The relative humidity is the weighted average with respect to liquid and ice. The longitudes of the simulations are indicated above each panel.

408 Figure ?? shows the equilibrium surface fluxes and surface precipitation in the GCM
 409 and LES. The latent heat flux decreases from about 300 W m^{-2} in deep convection re-
 410 gions to less than 100 W m^{-2} in shallow convection regions in the GCM. The sensible
 411 heat flux and net longwave radiative flux show similar differences between deep and shal-
 412 low convection regions, although the magnitudes are smaller. In the LES, the latent heat
 413 flux is weaker by 20–25% in deep convection regions, consistent with the higher relative
 414 humidity in the boundary layer (Figure ??b). The decrease in the latent heat flux is par-
 415 tially balanced by increases in the net upward longwave radiative flux and in the sen-
 416 sible heat flux, which result from an increase in the temperature difference between the
 417 surface and near-surface air. The differences in the sum of surface radiative and turbu-
 418 lent heat fluxes between the GCM and LES are 46 W m^{-2} and 38 W m^{-2} at 90.0° and
 419 112.5° longitudes, respectively. The surface energy budget is not closed in LES simula-
 420 tions with fixed surface temperatures; the results imply that significant changes in ocean

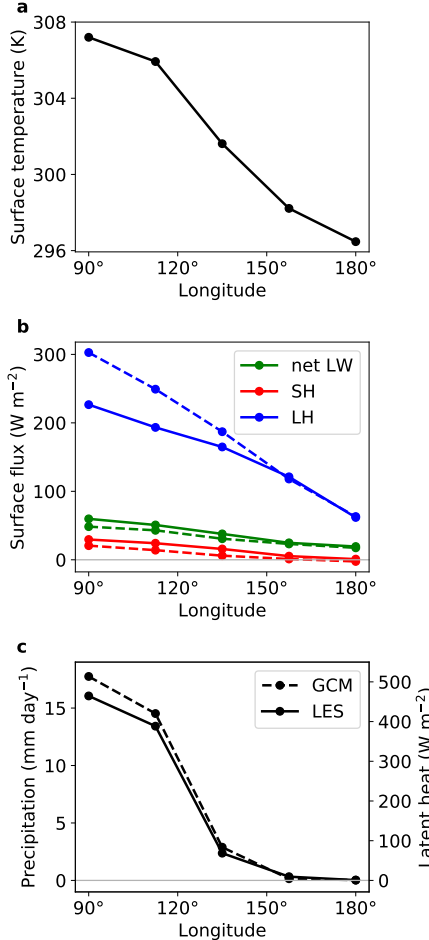


Figure 5. (a) Surface temperatures along the Walker circulation transect. (b) Equilibrium surface fluxes in the GCM (dashed) and LES (solid). Green lines denote net longwave radiative flux, red lines sensible heat flux, blue lines latent heat flux. (c) Surface precipitation in the GCM (dashed) and LES (solid). The latent heat associated with precipitation is shown on the right vertical axis.

heat uptake are required for LES simulations with a mixed-layer ocean to reach similar steady states. The surface fluxes in shallow convection regions are similar between the GCM and LES. The LES generally reproduces the spatial pattern of surface precipitation in the GCM, with strong precipitation in deep convection regions and weak or no precipitation in shallow convection regions along the transect. In deep convection regions, the surface precipitation is weaker in the LES than that in the GCM.

To further understand the difference between the GCM and LES, we compare vertically integrated moisture and dry enthalpy budgets (Figure ??). Note that the tendencies from horizontal advection in the LES are directly prescribed and are the same as those in the GCM. Since we focus on a statistically steady state, the sum of different terms affecting the budget is approximately zero. In deep convection regions, the moisture budget is kept in balance mainly by vertical advection, precipitation, and evaporation. The decreased evaporation in the LES is balanced by the decreased precipitation and the strengthened vertical advection of water vapor out of the moister boundary layer (Figure ??b).

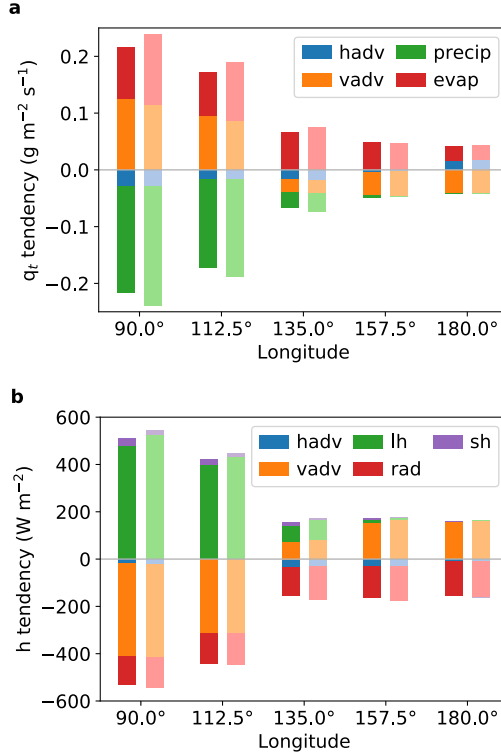


Figure 6. (a) Vertically integrated moisture tendencies from horizontal advection (hadv), vertical advection (vadv), precipitation (precip), and evaporation (evap). (b) Vertically integrated dry enthalpy tendencies from horizontal advection, vertical advection, latent heat of precipitation (lh), surface sensible heat flux (sh), and radiation (rad). Upward bars show sources and downward bars show sinks. LES and GCM budgets are shown in darker and lighter colors, respectively.

The dry enthalpy budget is kept in balance mainly by vertical advection, latent heat of precipitation, and radiation. The decrease in latent heat from precipitation in the LES is mainly balanced by the weaker radiative cooling and weaker adiabatic cooling from vertical motion. In the shallow convection regions, the main terms controlling the moisture budget are subsidence drying and evaporation, and the main terms controlling the dry enthalpy budget are subsidence warming and radiative cooling. The budgets are consistent between the GCM and LES in shallow convection regions.

Figure ?? shows the vertical profiles of different terms balancing moisture and temperature budgets at three longitudes along the Walker cell transect. At 90.0°, the moisture budget is mainly balanced by vertical advection and turbulent and convective drying, and the temperature budget is mainly balanced by vertical advection, turbulent and convective heating, and radiative cooling. The vertical structure of the tendencies is broadly consistent between the GCM and LES, with some differences in the boundary layer and near the melting level. The mismatch between the GCM and LES near the boundary layer top is related to the local minimum in moisture in the LES (Figure ??b). At 135.0°, all three physical terms (horizontal advection, vertical advection, and turbulence and convection) contribute to balancing the moisture budget. The dominant balance in the temperature budget is between subsidence warming, turbulent and convective heating, and radiative cooling. There are stronger mismatches between the GCM and LES in the free

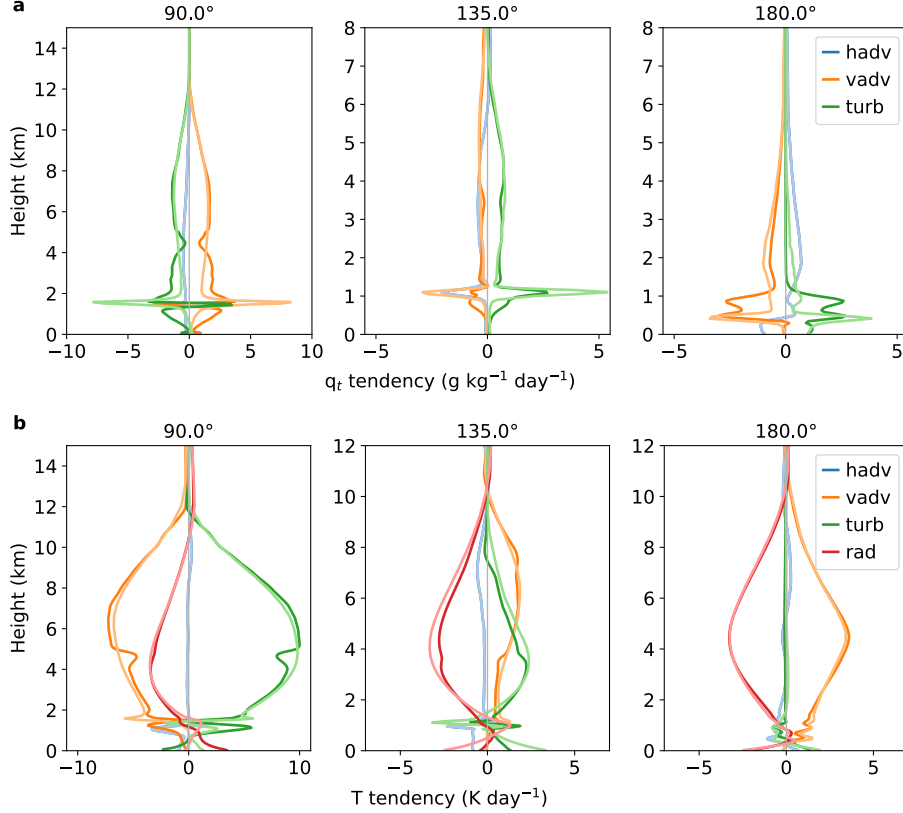


Figure 7. (a) Vertical profiles of moisture tendencies from horizontal advection (hadv), vertical advection (vadv), and turbulence and convection (turb). (b) Vertical profiles of temperature tendencies from horizontal advection, vertical advection, turbulence and convection, and radiation (rad). LES and GCM budgets are shown in darker and lighter colors, respectively. The longitudes of the simulations are indicated above each panel.

troposphere, which is related to the warm and dry biases in the GCM at 135.0° (Figure ??). At 180.0°, the dominant balance in the moisture budget is between subsidence drying and turbulent and convective moistening in the cloud layer, and subsidence drying and horizontal advection in the free troposphere. The GCM–LES difference in the moisture budget below 1 km suggests that the GCM has a shallower boundary layer and weaker convection than the LES, which is associated with the smaller surface buoyancy flux dominated by the weaker sensible heat flux in the GCM. The temperature budget is mainly balanced by subsidence warming and radiative cooling. The GCM and LES agree well on the temperature budget at 180.0°, as expected from the similar temperature profiles (Figure ??a).

Figure ?? shows the vertical profiles of cloud fraction and cloud water specific humidity along the Walker cell transect in the LES. The simulation with the coldest surface temperature (180.0°) produces a very shallow and thin cloud layer with cloud base around 300 m and cloud top around 1000 m. Below the cloud base, there is a well-mixed boundary layer, as seen in the vertical profiles of liquid-ice potential temperature and total water specific humidity (Figure ??). The well-mixed boundary layer and the shallow cumulus layer deepen as the surface temperature increases. The simulation at 135.0° longitude develops a secondary maximum in cloud fraction at about 4 km, which originates

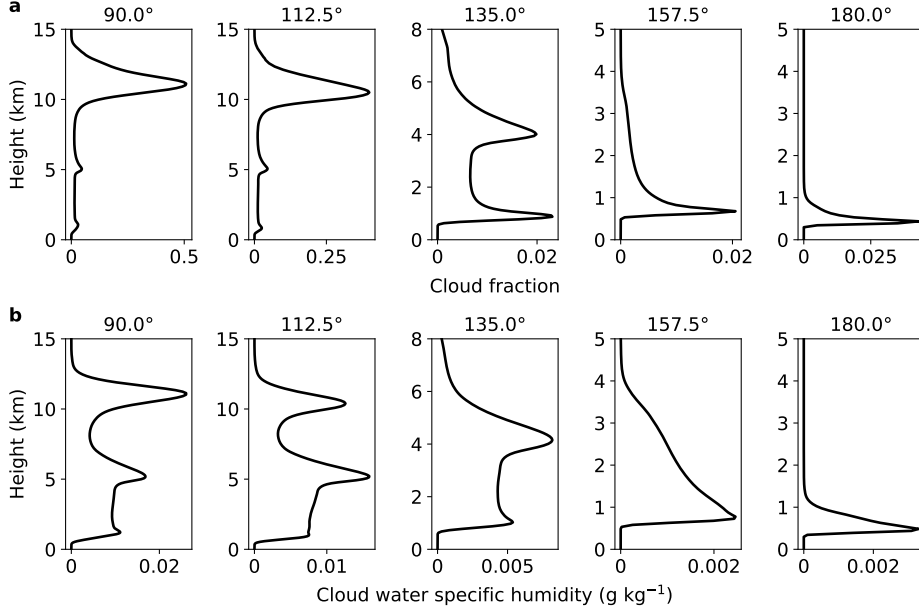


Figure 8. Vertical profiles of (a) cloud fraction and (b) cloud water specific humidity along the Walker circulation transect in the LES. The longitudes of the simulations are indicated above each panel.

from the cooling effects of snow melting. The cloud water specific humidity (the sum of the cloud liquid and ice specific humidities) has a similar vertical structure as the cloud fraction in shallow convection regions. As the surface temperature increases along the transect, the LES produce a transition to deep convection at 90.0° and 112.5° longitudes. The simulations produce anvil clouds with a peak in cloud fraction at about 11 km. There is a secondary maximum in cloud fraction near the melting level at about 5 km, which has also been reported in previous observational and high-resolution modeling studies (??, ??, ??). The vertical profile of cloud water specific humidity is more bottom-heavy than that of cloud fraction, with a more obvious peak near the melting level. In general, the LES produce little cloud ice in the upper troposphere in deep convection regions, which may be related to the relatively simple microphysics scheme and the lack of cloud-radiation interactions (??, ??) in this study.

5 Discussion and Conclusions

We have described a framework in which LES are driven by large-scale forcing taken from an idealized aquaplanet GCM, in a one-way coupling setup. The LES are forced with prescribed surface temperatures from the GCM, but they are otherwise freely evolving, without the direct constraints on temperature or humidity profiles that are usually imposed in LES studies. Instead, we imposed GCM-resolved, large-scale energy and moisture budget terms as forcing terms in the LES. We also imposed the large-scale pressure gradient from the GCM to drive the LES horizontal wind, and we relax the mean LES horizontal winds to those from the GCM to damp inertial oscillations that otherwise arise. Both the LES and GCM include the same radiative transfer schemes. This allows us to generate LES in grid columns of GCMs and to provide suitable benchmarks for testing and calibration of parameterization schemes in GCMs.

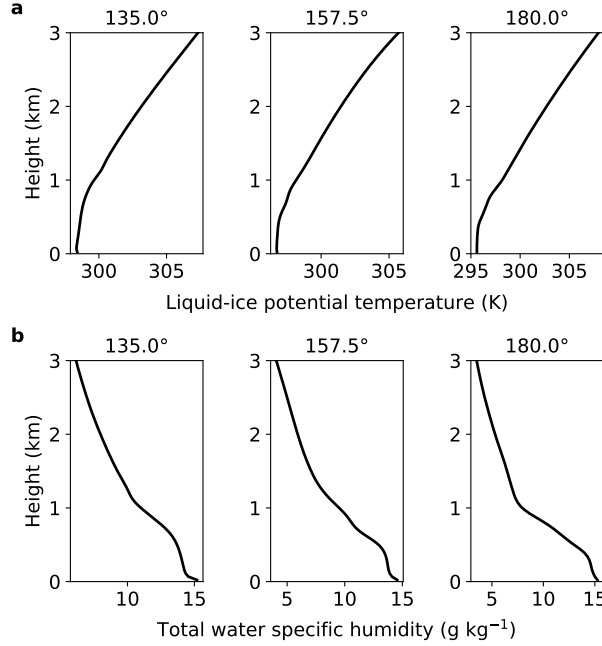


Figure 9. Vertical profiles of (a) liquid-ice potential temperature and (b) total water specific humidity in shallow convection regions. The longitudes of the simulations are indicated above each panel.

To illustrate the concepts, we used this forcing framework to simulate the transition from shallow to deep convection along an idealized Walker circulation transect. The Walker circulation is induced by prescribing a dipole structure of ocean heat flux convergence/divergence in the slab ocean of the GCM. LES driven by large-scale forcing from the GCM reach statistically steady states without nudging of thermodynamic variables toward reference profiles. The LES are able to reproduce the longitudinal variation of relative humidity, surface fluxes, and precipitation, with some mismatches to the GCM climatology, especially in deep convection regions. The mismatches are indicative of inadequacies in the GCM's convection parameterization, which is unsurprising given the simplicity of the parameterization. The mismatches can be used to systematically improve parameterization schemes, for example, with Bayesian calibration methods (?, ?, ?).

Our idealized setup has limitations. The gray radiation scheme we used to prove the concept does not depend on water vapor concentration or cloud properties. This distorts the radiative driving of the flows relative to what would happen in reality. The coupling of clouds, water vapor, and radiation has been shown to affect the Intertropical Convergence Zone and anvil clouds in deep convection regions (?, ?, ?, ?), as well as boundary layer clouds, the diurnal cycle of shallow cumulus, and the stratocumulus-to-cumulus transition (?, ?, ?). The resolution of LES used in this study (250 m) is not fine enough to fully resolve low clouds. Deep convective clouds are sensitive to microphysical processes, which are parameterized in a simple way in our model. These factors may contribute to the relatively small cloud fraction and cloud water path in our simulations of shallow cumulus, and to the relatively small amount of cloud ice in deep convection regions. These shortcomings limit the applicability of the results to some extent. But the simplifications facilitated the development and testing of the framework and suffice in

521 a proof-of-concept that illustrates its usability. They also simplify interpretation, for ex-
522 ample, of the cloud response to climate change.

523 We are currently using this framework to study cloud–climate feedbacks in an ide-
524 alized setting and to generate a library of LES simulations for developing and training
525 more comprehensive GCM parameterizations than the ones we used here. A library con-
526 taining a wide range of LES across different cloud regimes, including LES of changed cli-
527 mates, provides a powerful opportunity to systematically train complex dynamical pa-
528 rameterizations, with minimal imprinting of the GCM’s parameterizations onto the LES
529 forcing (the primary imprinting occurs through the dependence of the large-scale advec-
530 tion terms on the dynamical parameterizations). It thereby enables direct and meaning-
531 ful tests of the parameterizations against LES. An LES library including simulations of
532 changed climates not only enables tests of parameterizations but also provides an op-
533 portunity to investigate cloud feedbacks in LES that are not subject to nudging of ther-
534 modynamic variables to reference profiles or ad hoc assumptions about how large-scale
535 dynamics change with climate. The results of climate change simulations will be described
536 in a companion paper.

537 Appendix A Ocean Heat Flux

538 The time-independent ocean heat flux divergence (O) prescribed in the GCM is of
539 the following form:

$$540 \quad O(\phi, \eta) = Q_0 \left(1 - \frac{2\phi^2}{\phi_0^2} \right) \exp \left(-\frac{\phi^2}{\phi_0^2} \right) \\ 541 \quad - Q_1 \exp \left(-\frac{D(\eta, \eta_e)^2}{\eta_1^2} - \frac{(\phi - \phi_n)^2}{\phi_1^2} \right) + Q_1 \exp \left(-\frac{D(\eta, \eta_w)^2}{\eta_1^2} - \frac{(\phi - \phi_n)^2}{\phi_1^2} \right). \quad (A1)$$

544 Here, ϕ is latitude and η is longitude. The first term on the right-hand side represents
545 the hemispherically and zonally symmetric component of ocean heat flux divergence away
546 from the equator, as in ? (?) and ? (?). The second and third terms represent the zon-
547 ally asymmetric components, similar to ? (?). The asymmetric component of the heat
548 fluxes takes the form of a dipole in the northern hemisphere centered at $\phi_n = 15.0^\circ$ lat-
549 itude, with cooling and warming lobes centered at $\eta_w = 90.0^\circ$ and $\eta_e = 180.0^\circ$ longi-
550 tude. D is the distance between two longitudes η_a and η_b , defined as $D(\eta_a, \eta_b) = \min(|\eta_a - \eta_b|, 360^\circ - |\eta_a - \eta_b|)$.
551 The parameters we chose are $\phi_0 = 16.0^\circ$, $\eta_1 = 30.0^\circ$, $\phi_1 = 6.0^\circ$, $Q_0 = 50 \text{ W m}^{-2}$,
552 and $Q_1 = 150 \text{ W m}^{-2}$.

553 Appendix B Rayleigh damping

554 The Rayleigh damping coefficient (Γ_z) for horizontal velocities in the sponge layer
555 is

$$\Gamma_z = \begin{cases} \Gamma_{max} \sin^2 \left[\frac{\pi}{2} \left(1 - \frac{z_{top} - z}{z_d} \right) \right] & z \geq z_{top} - z_d, \\ 0 & z < z_{top} - z_d, \end{cases} \quad (B1)$$

556 where z_{top} is the depth of the LES domain (25.6 km) and z_d is the depth of the sponge
557 layer (8 km). Γ_{max} is set to 0.01 s^{-1} . The depth of the sponge layer does not significantly
558 affect the LES results.

559 Appendix C Microphysics

560 Our microphysics scheme is similar to Arctic mixed-phase scheme described in ?
561 (?) in that it is a one-moment microphysical parameterization with prognostic equations
562 for precipitating water and ice. Our microphysics differs from that in ? (?) primarily in
563 the liquid fraction function $\lambda(T)$, which determines the phase partitioning between cloud

562 liquid and ice:

$$563 \quad \lambda(T) = \begin{cases} 0 & T < T_i, \\ \frac{T-T_i}{T_f-T_i} & T_i < T \leq T_f, \\ 1 & T > T_f. \end{cases} \quad (C1)$$

564 Here, we use $T_i = 263.15$ K and $T_f = 273.15$ K. Further, our scheme replaces the cloud
 565 ice and snow auto-conversion rate closures used in ? (?) with those used in ? (?), which
 566 are more appropriate for use in simulations of subtropical and tropical convection.

567 **Acknowledgments**

568 We gratefully acknowledge the generous support of Eric and Wendy Schmidt (by re-
 569 commendation of Schmidt Futures), Mountain Philanthropies, EarthRise Alliance, Charles
 570 Trimble, the Paul G. Allen Family Foundation, and the National Science Foundation (grant
 571 1835860). The simulations were performed on Caltech’s High Performance Cluster, which
 572 is partially supported by a grant from the Gordon and Betty Moore Foundation. Part
 573 of this research was carried out at the Jet Propulsion Laboratory, California Institute
 574 of Technology, under a contract with the National Aeronautics and Space Administra-
 575 tion. The GCM codes are available on the GitHub repository https://github.com/szy21/fms_GCMForcing. The LES codes are available on the GitHub repository https://github.com/szy21/pycles_GCM/tree/shen2020. Primary GCM and LES data that may be
 576 used to produce the plots are available at <https://data.caltech.edu/records/1337>.
 577